https://doi.org/10.5194/amt-2021-290
Preprint. Discussion started: 5 October 2021
© Author(s) 2021. CC BY 4.0 License.

Atmospheric Measurement Techniques Discussions
Open Access
EGU

Simulated Multispectral Temperature and Atmospheric Composition Retrievals for the JPL GEO-IR Sounder

Vijay Natraj[1], Ming Luo[1], Jean-Francois Blavier[1], Vivienne H. Payne[1], Derek J. Posselt[1], Stanley P. Sander[1], Zhao-Cheng Zeng[2,3], Jessica L. Neu[1], Denis Tremblay[4], Longtao Wu[1], Jacola A. Roman[1], Yen-Hung Wu[1], Leonard I. Dorsky[1]

[1]Jet Propulsion Laboratory, California Institute of Technology, Pasadena, CA 91109, USA

[2]Joint Institute for Regional Earth System Science and Engineering, University of California, Los Angeles, CA 90095, USA

[3]Division of Geological and Planetary Sciences, California Institute of Technology, Pasadena, CA 91125, USA

[4]Global Science Technology, USA

Correspondence to: Vijay Natraj (vijay.natraj@jpl.nasa.gov)

Abstract. Satellite measurements enable quantification of atmospheric temperature, humidity, and trace gas vertical profiles. The majority of current instruments operate on polar orbiting satellites and either in the thermal/mid-wave or in the shortwave infrared spectral regions. We present a new multispectral instrument concept for improved measurements from geostationary orbit (GEO) with sensitivity to the boundary layer. The JPL GEO-IR sounder, which is an imaging Fourier Transform Spectrometer, uses a wide spectral range (1–15.4 μm), encompassing both reflected solar and thermal emission bands to improve sensitivity to the lower troposphere and boundary layer. We perform retrieval simulations for both clean and polluted scenarios that also encompass different temperature and humidity profiles. The results illustrate the benefits of combining shortwave and thermal infrared measurements. In particular, the former adds information in the boundary layer, while the latter helps to separate near-surface and mid-tropospheric variability. The performance of the JPL GEO-IR sounder is similar to or better than currently operational instruments. The proposed concept is expected to improve weather forecasting, severe storm tracking and forecasting, and also benefit local and global air quality and climate research.

https://doi.org/10.5194/amt-2021-290
Preprint. Discussion started: 5 October 2021
© Author(s) 2021. CC BY 4.0 License.

1 Introduction

The Program of Record (PoR) of current and planned satellite observations, as described in the 2017 US Earth Science Decadal Survey (*NASEM*, 2018), includes a range of spectrally-resolved radiance measurements in the thermal and shortwave infrared (TIR and SWIR) wavelength regions that provide key information on atmospheric temperature (TATM), water vapor (H_2O) and a range of trace gases (see Table 1 for a definition of spectral range designations). The TIR region can be further subdivided into midwave, longwave and very longwave infrared (MIR, LWIR and VLWIR) regions. Profiling of key gases including CO, CH_4, and CO_2 with sensitivity to planetary boundary layer (PBL) abundances was identified as a gap in current capability in the 2017 Decadal Survey, as was the promise of multispectral approaches for addressing this gap. In fact, combining radiances from the (thermal emission dominated) TIR and (solar reflection dominated) SWIR spectral regions has been shown to increase the vertical information content for these gases, providing improved information on near-surface variations relative to retrievals from the thermal alone (e.g., *Christi and Stephens*, 2004; *Worden et al.*, 2010; *Kuai et al.*, 2013; *Worden et al.*, 2015; *Fu et al.*, 2016; *Zhang et al.*, 2018; *Schneider et al.*, 2021). Such retrievals have the potential to extend the utility of satellite products for air quality forecasting, greenhouse gas monitoring and carbon cycle research. In addition, combining TIR and SWIR infrared radiances also offers opportunities for increasing the vertical information of H_2O retrievals in the PBL, another topic highlighted by the Decadal Survey and by the NASA Decadal Survey PBL Incubation Study Team (*Teixeira et al.,* 2021). Under clear-sky conditions, the SWIR provides sensitivity to H_2O (e.g., *Noël et al.*, 2005; *Trent et al.,* 2018; *Nelson et al.,* 2016), CO (e.g., *Buchwitz et al.,* 2004; *Deeter et al.,* 2009; *Landgraf et al.,* 2016; *Borsdorff et al.,* 2017; 2018), CH_4 (e.g., *Buchwitz et al.*, 2005; *Frankenberg et al*, 2006; *Yokota et al.*, 2009; *Hu et al*., 2018; *Parker et al*., 2020) and CO_2 (e.g., *Buchwitz et al.,* 2005; *Yokota et al*., 2009; *O'Dell et al*., 2018) throughout the full atmospheric column, providing complementary information to the TIR radiances that are strongly sensitive to the details of the profile of TATM, H_2O and trace gases but have variable sensitivity to the PBL, depending on surface and atmospheric conditions.

Table 2 shows a list of current and planned missions making spectrally-resolved, spaceborne TIR and SWIR measurements. In Low Earth Orbit (LEO), the MOPITT instrument on the Terra platform has been providing a record of TIR+SWIR CO for over two decades (*Buchholz et al.*, 2021). GOSAT and GOSAT-2 provide spectrally-resolved TIR and SWIR radiances on the same platform, with coverage of SWIR CO_2 and CH_4 bands, as well as H_2O absorption (*Trent et al.*, 2018), but not SWIR CO. The TROPOMI instrument on the Sentinel 5P satellite flies in formation with the CrIS instrument on the S-NPP satellite, providing near-coincident observations of TIR and SWIR, presenting opportunities for

https://doi.org/10.5194/amt-2021-290
Preprint. Discussion started: 5 October 2021
© Author(s) 2021. CC BY 4.0 License.

multispectral retrievals of CO and CH_4. Measurements from geostationary (GEO) orbit can provide contiguous horizontal (~4 km) and temporal (1–4 hours) resolution not possible from LEO. None of the current instruments/missions listed in Table 2 provide TIR + SWIR measurements from GEO on the same platform.

Here, we describe an instrument concept, called the JPL GEO-IR Sounder, that would provide profiling of TATM, H_2O, CO, CH_4 and CO_2, as well as numerous other species important for air quality and the hydrological cycle, from a geostationary platform. The JPL GEO-IR Sounder is an imaging Fourier transform spectrometer that utilizes high-speed digital focal plane arrays to record simultaneous TIR and SWIR spectra from each pixel of the array (640 ×480 or 1024×1024 format). The primary advantages of this sounder include the following:

- Coincident spatial and temporal retrievals of trace gases and TATM using both SWIR and TIR bands multiple times per day
- Combined TIR and SWIR retrievals provide for enhanced vertical resolution with PBL visibility for TATM, humidity and multiple trace gases
- Capability for retrievals of 4-D winds from combinations of cloud and H_2O temporal imagery as recently described using GIIRS data (*Ma et al*., 2021)
- Providing data products that are not readily obtained by combining retrievals from PoR LEO and GEO sounders.

This paper is organized as follows: in Section 2, we describe the scenarios used in the simulations. Section 3 provides brief descriptions of the radiative transfer (RT), instrument and inverse models. We discuss the considerations imposed on simulated JPL GEO-IR Sounder retrievals in Section 4. In Section 5, we present results for TATM, H_2O and trace gas retrievals from simulated GEO-IR Sounder measurements for both individual spectral regions and combinations. The relevance of these simulated retrievals for Observation System Simulation Experiments is discussed in Section 6. We arrive at some preliminary conclusions in Section 7. In particular, we show that the JPL GEO-IR Sounder would, for the first time, enable high spatial and temporal resolution simultaneous retrievals in the TIR and SWIR, which together provide more vertical profile information and improved sensitivity to the PBL than either spectral region alone.

2 Scenarios

Representative atmospheric conditions, including TATM, H_2O and pollutant distributions, surface temperature and other interferents are needed to understand satellite instrument performance. Using Weather Research and Forecasting model coupled to Chemistry (WRF-Chem) simulations at 4 km spatial

https://doi.org/10.5194/amt-2021-290
Preprint. Discussion started: 5 October 2021
© Author(s) 2021. CC BY 4.0 License.

resolution over the continental United States (Mary Barth, personal communication), we examined about 200 atmospheric profiles at six local times for two days in July 2006 over 17 locations that represent a range of diurnal meteorological conditions and a variety of air quality scenarios. For the purposes of these simulations, we assume clear-sky conditions. Simulation of conditions with significant aerosol loading and cloud interference adds significant complexity and is beyond the scope of this study. We calculate molecular absorption coefficients using the Line-By-Line Radiative Transfer Model (LBLRTM; *Clough et al.*, 2005).

The main goal of these simulations is to evaluate the retrieval characteristics of TATM, H_2O, and trace gases for different instrument configurations. From our database of over 200 summer-time atmospheric profiles over the continental US, we selected two representative daytime atmospheres; one near Houston to support the weather-focused OSSE analyses and the background trace gas case, and another in West Virginia that has more enhanced trace gas pollutants near the surface. Note that we kept the solar and viewing geometry as well as the surface albedo constant in order to isolate the effects of different boundary layer trace gas concentrations. Figure 1 shows the profile plots for TATM, H_2O, and trace gases that we examine in this manuscript (O_3, CO, CH_4 and CO_2) at the two locations.

The emissivity is obtained from a database structured by month and latitude/longitude coordinates. To populate the database, we used a global land use and land cover classification system developed by the U.S. Geological Survey (*Anderson et al.*, 1976) and mapped them into spectra from the ECOSTRESS spectral library (*Baldridge et al.*, 2009; *Meerdink et al.*, 2019; http://speclib.jpl.nasa.gov/), as described in the TES Algorithm Theoretical Basis Document (*Beer et al.*, 2002). The albedo is calculated from the emissivity using Kirchoff's law.

The location and times of the WRF-Chem profiles were used to calculate the solar viewing geometry, assuming a geostationary satellite at 95 W. The NOAA solar position calculator was used to verify the solar zenith and solar azimuth calculations (http://www.srrb.noaa.gov/highlights/sunrise/azel.html).

3 Models

3.1 Radiative transfer model

We use the accurate and numerically efficient two-stream-exact-single-scattering (2S-ESS) RT model (*Spurr and Natraj*, 2011; *Xi et al.*, 2015). This forward model is different from a typical two-stream model in that the two-stream approximation is used only to calculate the contribution of multiple scattering to the radiation field. Single scattering is treated in a numerically exact manner using all moments of the scattering phase function. High computational efficiency is achieved by employing the two-stream approximation for multiple scattering calculations. The exact single scattering calculation largely eliminates biases due to the severe truncation of the phase function inherent in a traditional two-stream approximation. Therefore, the 2S-ESS model is much more accurate than a typical two-stream model, and produces radiances and Jacobians that are typically within a few percent of numerically exact calculations and in most cases with biases much less than a percent. This model has been widely used for the remote sensing of greenhouse gases and aerosols (*Xi et al.*, 2015; *Zhang et al.*, 2015, 2016; *Zeng et al.*, 2017, 2018). Aerosols are not included in the analysis since the main objective was to investigate the impact of combining multiple spectral bands and of varying instrument parameters. However, the RT model has the capability of handling generic aerosol types.

The 2S-ESS RT model is used to generate monochromatic radiances at the top of the atmosphere for the atmospheric profiles and surface conditions near Houston over the entire spectral range considered for the JPL GEO-IR Sounder. Figure 2 shows the spectral radiance computed on a 0.002 cm^{-1} wavelength grid. We also calculate the individual contributions of each absorbing gas to the radiance. The gaseous absorption features have different spectral distributions and line strengths, which can be used to identify spectral windows for profile retrievals and recognize interfering gases that also absorb strongly in the same channels.

3.2 Instrument model

This section starts with a brief description of the spectrometer, primarily to define the terms used in the instrument model. We then detail the focal plane arrays and the optical filter that determine the bandpasses of the instrument. The processing steps of the instrument model are then explained. Finally, we show some of the resulting spectra produced by the model.

3.2.1 Optics Overview

The JPL GEO IR Sounder uses a Michelson interferometer, which modulates the light that passes through it. The interferometer is characterized by two main parameters: the spectral resolution, which is directly proportional to the maximum optical path difference (MOPD) between the two arms of the interferometer, and the optical throughput or étendue, which is given by the product of the area of the aperture stop and the angular field of view (AΩ). From geostationary orbit, a ground pixel of 2.1 km subtends an angle of 58.7 μrad and for a Focal Plane Array (FPA) of 1024×1024 pixels, the overall FOV is 60 mrad; this fits well within the Fourier Transform Spectrometer (FTS) design parameters. In parallel with the light from the target scene, a beam from an internal metrology laser travels through the interferometer. This laser is used to precisely measure the optical path difference, to within a small fraction of the laser wavelength. An imaging FTS (IFTS) shares many of the principles of the traditional FTS, the main difference is that the detector is replaced with an FPA. The main challenge in the IFTS

© Author(s) 2021. CC BY 4.0 License.

design is in the FPA, which must operate at high frame rate (0.5–1 kHz) and at high dynamic range (14–16 bits) to properly digitize the interferograms.

3.2.2 Focal Plane Arrays

The JPL GEO-IR Sounder FPA optics uses a dichroic to split the interferometer output along the wavelength dimension: radiation from 1 µm to 5.3 µm is sent towards FPA #1 and radiation from 5.3 µm to 15.4 µm is directed to FPA #2. Whereas FPA #2 is a single-color detector, handling its full domain at all times, FPA #1 is a dual-color detector. The two colors of FPA #1 are operated sequentially: recording either the 1 µm to 3 µm domain (SWIR; FPA #1a) or the 3 µm to 5.3 µm domain (MWIR; FPA #1b). This dual-color operation is implemented inside the FPA by having two distinct detectors in an optical "sandwich". It is designed to minimize the effect of photon noise in the low-light MWIR and SWIR domains. Furthermore, the SWIR FPA #1a bandpass is narrowed by a triple-band optical filter, tailored to the regions that contain absorption bands of interest (Figure 3). As listed in Table 3, the SWIR domains of interest are: (1) 4210–4350 cm^{-1}, (2) 4810–4900 cm^{-1}, (3) 6000–6150 cm^{-1} and (4) 6170–6290 cm^{-1}. Based on previous optical filter studies, we allow 200 cm^{-1} for the filter slope on either side. Since the gap between the first two domains would therefore be small, and the signal there is low, these have been merged (4210–4900 cm^{-1}). Domains (3) and (4) have also been combined (6000–6290 cm^{-1}). In addition, the 1.27 µm oxygen band (7780–8010 cm^{-1}) will be used to measure the light path. We believe that it is best to specify the 50% transmission points for the filter bands, as that is where the slope is maximum and hence most easily verified. With a 200 cm^{-1} transition region, the 50% point will be 100 cm^{-1} outside of the bandpasses. Hence the final triple-band filter configuration is: 4110–5000 cm^{-1} (2.000–2.433 µm), 5900–6390 cm^{-1} (1.565–1.695 µm), 7680–8110 cm^{-1} (1.233–1.302 µm). The triple-band filter physically covers the two-color FPA #1. It is intended to limit the photon flux only in the SWIR mode of operation, with the detector that is sensitive over the 1–3 µm domain (FPA #1a). The filter must also be transparent over the 3–5.3 µm domain of the other shared detector (FPA #1b). It may be possible to combine the first band of the triple-band filter (2–2.433 µm) with this MWIR transparency need (3–5.3 µm) but this has not been simulated in this study.

3.2.3 Instrument Model Description

The Instrument Model for the JPL GEO IR Sounder allows us to explore the instrument trade space and its effect on retrieved atmospheric composition. It includes the ability to convolve synthetic spectra and Jacobians with the instrument line shape (ILS). The model performs the following steps:

1. Reads synthetic data from the radiative transfer model. The radiance spectrum is extended using blackbody curves simulating the Earth and the Sun, and converted to a photon flux spectrum. After this step, the spectrum is in units of photons/m^2/sr/cm^{-1}/s.

https://doi.org/10.5194/amt-2021-290
Preprint. Discussion started: 5 October 2021
© Author(s) 2021. CC BY 4.0 License.
Atmospheric Measurement Techniques Discussions

2. Convolves the spectrum with the theoretical FTS ILS, given as: 2Lsinc(2σL), where L is the MOPD and sinc(x)=sin(πx)/πx. This expression of the ILS has unit area, and hence the convolution does not change the overall magnitude or the units of the spectrum. It does, however, reduce the spectral resolution, broadening all sharp features. In the same step, we resample the spectrum on a coarser grid, i.e., we "decimate" the spectrum. For example, in the current simulations, we reduce the wavenumber interval by a factor of 50, from 0.002 cm^{-1} to 0.1 cm^{-1}.

3. Scales the spectrum by the étendue of the instrument. After this step, the units of the spectrum are photons/cm^{-1}/s.

4. Applies further scaling to account for the single output design (where half the light is sent through the instrument and the other half sent back to the source), losses in the metallic coatings and at the uncoated optical interfaces (i.e., compensator and back side of beamsplitter), the efficiency of the beamsplitter coating, the quantum efficiency of the detector, and the integration time of the analog-to-digital converter. After this step, the units of the spectrum are photoelectrons/cm^{-1}.

5. Applies bandpass limits caused either by an optical filter or the working domain of the detector.

6. Applies the Fourier transform to convert the spectrum into an interferogram.

7. Computes the number of photoelectrons counted in each interferogram data sample. From this, we can compute the photon noise. Subsequently, white noise is added to the interferogram with a root mean square amplitude matching the computed photon noise.

8. Simulates the interferogram digitization, performed for each pixel within the Read Out Integrated Circuit of the two FPAs.

9. Produces the final spectrum by Fourier transform. The signal to noise ratio (SNR) is then evaluated by computing the noise level in blacked-out regions on either side of the instrument bandpass, and by locating the maximum signal within the bandpass.

3.2.4 Spectral Results

Figure 3 shows a JPL GEO-IR Sounder model spectrum for FPA #1a, covering the SWIR domain. Figure 4 shows a similar spectrum for the VLWIR, LWIR and MWIR FPA bands: FPA #2 covers the VLWIR and LWIR domains, and FPA #1b covers the MWIR domain. The spectral ranges include the range utilized by existing TIR sounders (AIRS, CrIS, IASI) and selected bands in the SWIR. In particular, the FPA #2 spectral range contains critical information for radiance assimilation by weather forecasting algorithms (see, e.g., *Eresmaa et al.*, 2017). The spectral resolution (MOPD) of the JPL GEO-IR Sounder is configurable. For these simulations, we choose to look at three possible MOPD options: a CrIS-like spectral resolution (0.8 cm MOPD, 0.625 cm^{-1} resolution, described as nominal spectral resolution or NSR in Table 4), an intermediate option (2 cm MOPD, 0.25 cm^{-1} resolution), and a high spectral

https://doi.org/10.5194/amt-2021-290
Preprint. Discussion started: 5 October 2021
© Author(s) 2021. CC BY 4.0 License.

resolution option (5 cm MOPD, 0.1 cm^{-1} resolution, described as full spectral resolution or FSR in Table 4). In order to make for an "apples to apples" comparison, we consider the same integration time (1 millisecond per interferogram point) for these three options. The integration time is driven by the high spectral resolution option. The native and binned (footprint-averaged) ground sampling distance (GSD) are also indicated in Table 4.

3.3 Inverse model

We use an optimal estimation approach (*Rodgers*, 2000) and perform linear retrievals from simulated radiances described in the previous section. The spectral differences of the modeled and the satellite measured radiances and the differences of the species profile and the *a priori* profile are mathematically minimized, weighted by the measurement error and the *a priori* constraint. The species profile can then be derived optimally.

The *a priori* constraint vectors for TATM and H_2O are obtained from forecast fields from the NASA Global Modeling and Assimilation Office, supplied for use within the TES retrieval algorithm (*Bowman et al.*, 2006). *A priori* constraint matrices are constructed, using the method described in *Kulawik et al.* (2006), from an altitude-dependent combination of zeroth, first and second order derivatives of the profiles. For TATM and H_2O, the square roots of the diagonals of the respective constraint matrices are on the order of 1.8–2.2 K and 15–18%, respectively. *A priori* vectors for O_3, CO and CH_4 are taken from calculations using the Model for OZone And Related chemical Tracers (MOZART3) (*Brasseur et al.*, 1998; *Park et al.*, 2004) that were performed for the purpose of construction of trace gas climatologies for the Aura mission. For O_3, the square root of the diagonal of the constraint matrix is on the order of 25% in the troposphere, 40% in the stratosphere and 15% above. For CO, this is set to 30% over the entire atmosphere, while for CH_4, the values range from 2–10%. The constraint matrices for CO are the same as those used by the MOPITT algorithm (*Deeter et al.*, 2010). For CO_2, the *a priori* vector and constraint used are described in *Kulawik et al.* (2010). The square root of the diagonal of the constraint matrix ranges from 1.2–2%. We note that these profile constraints were developed for TIR instruments, and may therefore not capture strong near-surface variability. There could be scope for increasing the near-surface information content via development of updated constraints, although that work is outside of the scope of this study.

The end-to-end retrieval analysis provides averaging kernels, which describe the sensitivity of the retrieved atmospheric state to the true state; degrees of freedom for signal (DOFS), which denote the pieces of vertical information contained in the retrieved profile; and retrieval errors. These metrics are used for evaluating the retrieval results for a variety of spectral bands, and spectral and spatial resolutions.

https://doi.org/10.5194/amt-2021-290
Preprint. Discussion started: 5 October 2021
© Author(s) 2021. CC BY 4.0 License.

Atmospheric Measurement Techniques Discussions

4 Considerations for simulated retrievals

For the retrieval simulations described here, we consider a somewhat idealized scenario. Simulations have been performed for clear-sky conditions, with no aerosols in the scenes. In retrievals from actual measured radiances, even for a clear-sky, non-scattering atmosphere, there is always some forward model error due to, e.g., uncertainties in spectroscopy, interfering species and the treatment of the surface. With real data, these kinds of uncertainties can lead to significant systematic errors in the retrievals, particularly for well-mixed greenhouse gases such as CH_4 and CO_2. For the simulations presented here, we have considered only the error term associated with measurement noise.

The measurement noise associated with the simulated radiance is obtained using the instrument model described in Section 3.2. The JPL GEO-IR sounder concept is configurable in terms of spectral range and spectral resolution, with a native spatial resolution that corresponds to a 2.1 km footprint on the ground. Different configurations of the instrument concept will affect the number of photons available in each channel and therefore impact the signal to noise. For a given integration time, lower spectral resolution leads to correspondingly higher SNR. The SNR of the observed radiance spectra can be increased by increasing the integration time. For geostationary observations, this leads to a trade-off between measurement noise and temporal resolution. An increase of the throughput (etendue) leads to lower noise (*Schwantes et al.*, 2002).

In retrievals from real data, higher spectral resolution can offer advantages in terms of ability to distinguish between the target molecule and interfering spectral signatures from other molecules with features in the spectral range of interest, despite the increase in measurement noise. In the results presented in this study, that advantage in reduction of systematic error is not accounted for. The SNR can also be increased by aggregating spatially. For example, aggregating four 2.1 km footprints would increase the SNR by a factor of two. Depending on the application of the measurements, there may be some advantage to trading spatial resolution for a gain in SNR.

5 Results

5.1 TATM and H_2O retrievals

High spectral resolution is necessary to provide the vertically resolved TATM and H_2O information critical for numerical weather prediction and for many other applications including local extreme weather conditions and global climate change. Current satellite-based TATM and H_2O retrievals mainly utilize TIR spectral measurements. Here we also examine information gained from adding SWIR measurements. Tables 5 and 6 list the possible choices of frequency range for TATM and H_2O retrievals. Some of these spectral ranges are used in current operational missions, while some are candidates for future missions.

https://doi.org/10.5194/amt-2021-290
Preprint. Discussion started: 5 October 2021
© Author(s) 2021. CC BY 4.0 License.

We compare results for three values of spectral resolution and for two values of spatial resolution.

Examining the above DOFS tables, we see competing effects of spectral resolution (MOPD) and measurement noise. As described in Section 3.2, the measurement noise (Noise Equivalent Spectral Radiance, NESR) is estimated for a fixed integration time for both the 2.1 and 4.2 km ground sampling distance (GSD) configurations. The NESR for the MOPD = 0.8 cm instrument is therefore smaller than that for the MOPD = 2 or 5 cm instruments. Typically, however, the higher spectral resolution instruments provide larger DOFS than the NSR instrument. For H_2O retrievals, the optimal DOFS are provided by the intermediate resolution instrument.

The differences in DOFS for the two GSD values are obvious. This shows the trade-off between spatial resolution and retrieval vertical resolution and precision (not listed). Both GSDs provide high precision, high vertical resolution TATM and H_2O retrievals. We estimate the tropospheric vertical resolution for TATM to be 1.5–2 km with <0.5 K precision, and for H_2O to be 1–2 km with ~5% precision. In comparison, representative tropospheric values for AIRS are 1 km for TATM and 2 km for H_2O (*Irion et al.*, 2018).

The selection of spectral regions also affects the TATM and H_2O products. For example, using the VLWIR+LWIR+MWIR domain provides much more sensitivity compared to using MWIR alone. Figure 5 shows averaging kernel plots for TATM and H_2O for the 4.2 km GSD option for four spectral band combinations: VLWIR+LWIR, MWIR, SWIR, and VLWIR+LWIR+MWIR+SWIR. The characteristics of the TIR TATM and H_2O retrievals are very similar to those obtained by currently operating instruments. We note that the sensitivity of SWIR retrievals is mostly near the surface. Further, the measurement noise in the SWIR was reduced by a factor of 5 in these figures by averaging 25 pixels, thereby reducing the effective GSD to 21 km. Note that this is worse than the 15 km AIRS/CrIS native resolution but better than the 45 km that the TATM and H_2O products are typically reported on.

5.2 Trace gas retrievals

Among many possible detectable trace gases from the extended spectral radiance measurements, we selected to examine profile retrieval characteristics for O_3, CO, CH_4 and CO_2 for the given instrument configurations (see Table 3 for retrieval spectral ranges). Table 7 lists DOFS for the chosen trace gases for the West Virginia scenario. Results for the FSR option are largely similar to those for the intermediate spectral resolution instrument and are hence not shown. The DOFS in Table 7 are broadly consistent with previously published work on species profile retrievals from satellite observations (*Beer*, 2006; *Connor et al.*, 2008; *Deeter et al.*, 2009, 2015; *George et al.*, 2009; *Kulawik et al.*, 2010; *Worden et al.*, 2010, 2013; *Clerbaux et al.*, 2015; *Fu et al.*, 2016; *Smith and Barnet*, 2020). For a given spectral resolution instrument, the higher DOFS in retrievals for the larger GSD case for all species are due to

https://doi.org/10.5194/amt-2021-290
Preprint. Discussion started: 5 October 2021
© Author(s) 2021. CC BY 4.0 License.

the reduced measurement noise. For a given GSD, the DOFS are slightly higher for the NSR case compared to the MOPD = 2 cm case, but the differences are small. It is worth reiterating that these simulated retrievals represent an idealized scenario, where we assume perfect knowledge of interfering species in the spectral range for any given target species. In this scenario, with a constant integration time, the NSR option provides similar results to the MOPD = 2 cm option due to the trade-off between spectral resolution and instrument noise.

Figure 6 shows averaging kernel plots for CO for MWIR- and SWIR-only scenarios and for combined MWIR+SWIR retrievals. The combination of wavelength regions provides improved sensitivity to the lower troposphere compared to either spectral region alone. CO_2 retrievals (Figure 7) benefit the most from the combination of VLWIR+MWIR+SWIR retrievals. The SWIR domain adds sensitivity in the lower troposphere and near the surface. The characteristics of the CO_2 retrievals are in good agreement with OCO-2/3 observations. For CH_4 (Figure 8), the addition of SWIR bands also provides noticeable enhancement in lower tropospheric and near-surface sensitivity. For CO retrievals, the contribution of the SWIR to the near-surface sensitivity is less pronounced. The stronger contribution of SWIR measurements to the total DOFS for CH_4 and CO_2 compared to CO is a result of three factors: (1) lower top of the atmosphere solar irradiance in the CO spectral region relative to the CH_4 and CO_2 regions, (2) lower surface albedo, and (3) larger absorption, primarily by H_2O and CH_4. Our results for O_3 are broadly consistent with published results for LWIR satellite observations (e.g., *Nassar et al.*, 2008; *Smith and Barnet*, 2020). Figures 6–8 use the same effective GSD of 21 km in the SWIR as described in Section 5.1.

6 Use of synthetic retrievals in Observation System Simulation Experiments

Observing system simulation experiments (OSSEs) are used to assess the potential information in a new set of measurements before they are deployed. In the case of satellite remote sensing, there are several types of experiment that may be performed (*Zeng et al.*, 2020): a sampling OSSE, in which an orbit simulator is used to determine how often the observing system views features of interest (e.g., *Crespo et al.*, 2017); a geophysical variable (or retrieval) OSSE, in which synthetic measurements are used to estimate synthetic geophysical variables and their uncertainties (e.g., *Xu et al.*, 2019 and this manuscript); and impact OSSEs, the most common of which are those that assess the effect of assimilation of new measurements on a weather forecast (e.g., *Hoffman and Atlas*, 2016; *Posselt et al.*, 2021). This paper describes a set of geophysical variable/retrieval OSSEs, and the observing system characteristics (spatial and temporal resolution and uncertainties).

https://doi.org/10.5194/amt-2021-290
Preprint. Discussion started: 5 October 2021
© Author(s) 2021. CC BY 4.0 License.

The detailed characterization of uncertainties in the retrieved TATM and H_2O retrievals provided by this study will be directly incorporated into a set of weather forecast OSSEs, the results of which will be reported in a subsequent paper. Note that, for a weather forecast OSSE to be credible, it is crucial to represent the synthetic measurements as accurately as possible. TATM and H_2O precision and total error are reported in Table 8; it can be seen that the errors for the MWIR-only configuration are on the order of the errors in CrIS and AIRS retrievals, while the full-spectrum JPL GEO-IR Sounder configuration yields total errors that are smaller than those from either CrIS or AIRS. As such, assimilation of information from JPL GEO-IR Sounder measurements is expected *a priori* to have as much or greater impact on weather forecasts compared with existing hyperspectral sounders. Note that the total error in the full-spectral-range TATM and H_2O retrievals is equivalent to, or less than, the uncertainty reported for radiosonde measurements of these quantities (*Rienecker et al.*, 2008; Table 3.5.2).

While it is common to assimilate radiances (rather than retrieved TATM and H_2O) in modern data assimilation systems, this is not necessarily the right choice in an OSSE. This is because radiance assimilation necessitates careful tuning of the radiative transfer model to remove bias and to make it consistent with the model processes and resolution. This is an iterative and time consuming process that requires comparison with other measurements. In addition, the true state (from the nature run) is available in an OSSE. This means that an unbiased mapping from measurements to state space is straightforward, in contrast to real measurements. If the TATM and H_2O retrieval algorithm can be used to apply the resolution and noise characteristics to the nature run profiles, then assimilation of retrievals is a more straightforward and more realistic option.

Finally, we note that there will be particular advantages and challenges in assimilating the high temporal resolution data that will be available from the JPL GEO-IR Sounder. The clear advantage is the ability to observe rapidly evolving processes (e.g., the environment around thunderstorms and hurricanes). This information is not available from the current LEO constellation. However, modern data assimilation systems are configured for assimilation of intermittent data (at best hourly in operational data assimilation systems) and will require modification to make best use of the high time frequency geostationary soundings provided by the JPL GEO-IR Sounder.

7 Conclusions

In this paper, we present an end-to-end retrieval study for a proposed FTS instrument covering the entire infrared spectral range from 1–15 μm from a geostationary satellite orbit. An instrument model is used to derive realistic measurement radiance and noise for several diurnal observations over small ground footprints (e.g., 2.1 km). We perform TATM and trace gas profile retrievals for the JPL GEO-IR

Sounder that covers the entire VLWIR, LWIR, MWIR and SWIR spectral domains. Retrieval characteristics, such as DOFS and measurement error, are examined in order to evaluate the performance of several instrument configurations. These configurations include VLWIR-, LWIR-, MWIR-, and SWIR-only and their combinations, and different spectral and spatial resolutions, for a realistic geostationary observing system making field-of-view observations at fixed time intervals. Two summer-time atmospheres are used: a scenario near Houston as a clean-air case, and one in West Virginia representing a polluted scenario. We analyze TATM, H_2O, O_3, CO, CH_4 and CO_2 profile retrievals.

High spectral resolution can provide improved ability to distinguish absorption lines of the target species from interferents. In the case of species (such as O_3) where much of the total column lies in the stratosphere, higher spectral resolution also provides enhanced ability to separate the tropospheric signal from the stratospheric signal. When the total integration time is fixed, there is a trade-off between spectral resolution and noise. In the idealized retrievals presented here, we assume perfect knowledge of interfering species. In this case, three different MOPDs provide comparable results in terms of DOFS. However, in the real world, we would expect higher spectral resolution to offer advantages in terms of reduction in systematic errors.

Compared to single spectral region instruments, e.g., only LWIR or MWIR, combinations of VLWIR/LWIR/MWIR/SWIR enhance the sensitivity of the retrievals to the lower troposphere. In our analyses, we find that the contributions from the SWIR in the combined measurements are noticeable for both trace gas and TATM retrievals, especially when the ground pixels are averaged to reduce measurement noise in the SWIR. In particular, the SWIR measurements add information in the lower troposphere and for near-surface species retrievals.

We limit the spatial resolution choices to GSD = 2.1 km and 4.2 km in our simulations. Especially for multi-band retrievals, the results are realistically adequate for many research applications for both ground sampling footprints. We compare performance metrics (e.g., NESR and SNR) for the proposed instrument with values for several current/past satellite instruments in multiple spectral bands. The performance of the JPL GEO-IR Sounder is similar to or better than currently operational instruments. At the same time, the JPL GEO-IR Sounder provides much higher spatial and temporal resolution and a wider range of trace gases than current instruments that combine TIR and SWIR. The derived retrieval characteristics (e.g., DOFS and retrieval errors) also compare favorably with currently available products.

Data availability

The code and data are available from the authors upon request.

https://doi.org/10.5194/amt-2021-290
Preprint. Discussion started: 5 October 2021
© Author(s) 2021. CC BY 4.0 License.

Atmospheric Measurement Techniques
Discussions

Author contributions

SPS, Y-HW and LID conceived the work. VN provided the radiative transfer model, led the simulated retrieval work, and prepared the manuscript. ML, J-FB and ZZ assisted with the retrievals. ML provided the trace gas absorption and inverse models. JLN provided the profiles for the simulations. SSK provided the emissivity database and advised on the retrieval constraints. J-FB provided the instrument model. VHP and SPS helped analyze the simulation results. LW, JAR and DJP provided the connection with OSSEs. All listed authors contributed to the review and editing of this manuscript.

Competing interests

The authors declare that they have no conflict of interest.

Acknowledgements

A portion of this research was carried out at the Jet Propulsion Laboratory, California Institute of Technology, under a contract with the National Aeronautics and Space Administration (80NM0018D0004). The authors acknowledge S. Kulawik for helpful discussions on retrieval constraints.

Financial Support

The authors acknowledge support from the National Oceanic and Atmospheric Administration through BAA-NOAA-GEO-2019, and the Jet Propulsion Laboratory Advanced Concepts Program.

https://doi.org/10.5194/amt-2021-290
Preprint. Discussion started: 5 October 2021
© Author(s) 2021. CC BY 4.0 License.

References

Anderson, J. R., Hardy, E. E., Roach, J. T., and Witmer, R. E.: A land use and land cover classification system for use with remote sensor data, USGS Tech Rep., https://doi.org/10.3133/pp964, 1976.

Baldridge, A. M., S. J. Hook, C. I. Grove, and G. Rivera: The ASTER spectral library version 2.0, Remote Sens. Environ., 113(4), 711–715, https://doi.org/10.1016/j.rse.2008.11.007, 2009.

Beer, R., Bowman, K. W., Brown, P. D., Clough, S. A., Eldering, A., Goldman, A., Jacob, D. J., Lampel, M., Logan, J. A., Luo, M., Murcray, F. J., Osterman, G. B., Rider, D. M., Rinsland, C. P., Rodgers, C. D., Sander, S. P., Shepard, M., Sund, S., Ustinov, E., Worden, H. M., and Worden, J.: Tropospheric Emission Spectrometer (TES) level 2 algorithm theoretical basis document, Version 1.15, JPL D-16474, Jet Propulsion Laboratory, Pasadena, California (available at https://eospso.gsfc.nasa.gov/atbd-category/53), 2002.

Beer, R.: TES on the Aura mission: Scientific objectives, measurements, and analysis overview, IEEE Trans. Geosci. Remote Sens., 44(5), 1102–1105, https://doi.org/10.1109/TGRS.2005.863716, 2006.

Bowman, K. W., Rodgers, C. D., Kulawik, S. S., Worden, J., Sarkissian, E., Osterman, G., Steck, T., Luo, M., Eldering, A., Shephard, M., Worden, H., Lampel, M., Clough, S., Brown, P., Rinsland, C., Gunson, M., and Beer, R.: Tropospheric Emission Spectrometer: Retrieval method and error analysis, IEEE Trans. Geosci. Remote Sens., 44(5), 1297–1307, https://doi.org/10.1109/TGRS.2006.871234, 2006.

Borsdorff, T., Aan de Brugh, J., Hu, H., Aben, I., Hasekamp, O., and Landgraf, J.: Measuring carbon monoxide with TROPOMI: First results and a comparison with ECMWF-IFS analysis data, Geophys. Res. Lett., 45(6), 2826–2832, https://doi.org/10.1002/2018GL077045, 2018.

Borsdorff, T., aan de Brugh, J., Hu, H., Nédélec, P., Aben, I., and Landgraf, J.: Carbon monoxide column retrieval for clear-sky and cloudy atmospheres: A full-mission data set from SCIAMACHY 2.3 μm reflectance measurements, Atmos. Meas. Tech., 10(5), 1769–1782, https://doi.org/10.5194/amt-10-1769-2017, 2017.

Brasseur, G. P., Hauglustaine, D. A., Walters, S., Rasch, P. J., Muller, J. F., Granier, C., and Tie, X. X.: MOZART, a global chemical transport model for ozone and related chemical tracers 1. Model description, J. Geophys. Res., 103(D21), 28265–28289, https://doi.org/10.1029/98JD02397, 1998.

Buchholz, R. R., Worden, H. M., Park, M., Francis, G., Deeter, M. N., Edwards, D. P., Emmons, L. K., Gaubert, B., Gille, J., Martinez-Alonso, S., Tang, W., Kumar, R., Drummond, J. R., Clerbaux, C., George, M., Coheur, P.-F., Hurtmans, D., Bowman, K. W., Luo, M., Payne, V. H., Worden, J. R., Chin, M., Levy, R. C., Warner, J., Wei, Z., and Kulawik, S. S.: Air pollution trends measured from Terra: CO and AOD over industrial, fire-prone, and background regions, Remote Sens. Environ., 256, 112275, https://doi.org/10.1016/j.rse.2020.112275, 2021.

Buchwitz, M., de Beek, R., Bramstedt, K., Noël, S., Bovensmann, H., and Burrows, J. P.: Global carbon monoxide as retrieved from SCIAMACHY by WFM-DOAS, Atmos. Chem. Phys., 4(7), 1945–1960, https://doi.org/10.5194/acp-4-1945-2004, 2004.

Buchwitz, M., de Beek, R., Noël, S., Burrows, J. P., Bovensmann, H., Bremer, H., Bergamaschi, P., Körner, S., and Heimann, M.: Carbon monoxide, methane and carbon dioxide columns retrieved from SCIAMACHY by WFM-DOAS: Year 2003 initial data set, Atmos. Chem. Phys., 5(12), 3313–3329, https://doi.org/10.5194/acp-5-3313-2005, 2005.

Christi, M. J., and Stephens, G. L.: Retrieving profiles of atmospheric CO_2 in clear sky and in the presence of thin cloud using spectroscopy from the near and thermal infrared: A preliminary case study, J. Geophys. Res., 109(D4), D04316, https://doi.org/10.1029/2003jd004058, 2004.

Clough, S. A., Shephard, M. W., Mlawer, E., Delamere, J. S., Iacono, M., Cady-Pereira, K., Boukabara, S., and Brown, P. D.: Atmospheric radiative transfer modeling: a summary of the AER codes, J. Quant. Spectrosc. Radiat. Transfer, 91(2), 233–244, https://doi.org/10.1016/j.jqsrt.2004.05.058, 2005.

Connor, B. J., Boesch. H., Toon, G., Sen, B., Miller, C., and Crisp, D.: Orbiting Carbon Observatory: Inverse method and prospective error analysis, J. Geophys. Res., 113, D05305, https://doi.org/10.1029/2006JD008336, 2008.

https://doi.org/10.5194/amt-2021-290
Preprint. Discussion started: 5 October 2021
© Author(s) 2021. CC BY 4.0 License.
Atmospheric Measurement Techniques Discussions

Crespo, J. A., Posselt, D. J., Naud, C. M., and Bussy-Virat, C.: Assessing CYGNSS's potential to observe extratropical fronts and cyclones, J. Appl. Meteor. Climatol., 56(7), 2027–2034, https://doi.org/10.1175/JAMC-D-17-0050.1, 2017.

Clerbaux, C., Hadji-Lazaro, J., Turquety, S., George, M., Boynard, A., Pommier, M., Safieddine, S., Coheur, P.-F., Hurtmans, D., Clarisse, L., and Van Damme, M.: Tracking pollutants from space: Eight years of IASI satellite observation, C. R. Géosci., 347(3), 134–144, https://doi.org/10.1016/j.crte.2015.06.001, 2015.

Deeter, M. N., Edwards, D. P., Gille, J. C., and Drummond, J. R.: CO retrievals based on MOPITT near-infrared observations, J. Geophys. Res., 114(D4), D04303, https://doi.org/10.1029/2008JD010872, 2009.

Deeter, M. N., Edwards, D. P., Gille, J. C., Emmons, L. K., Francis, G., Ho, S.-P., Mao, D., Masters, D., Worden, H. M., Drummond, J. R., and Novelli, P. C.: The MOPITT version 4 CO product: Algorithm enhancements, validation, and long-term stability, J. Geophys. Res., 115(D7), D07306, https://doi.org/10.1029/2009JD013005, 2010.

Deeter, M. N., Edwards, D. P., Gille, J. C., and Worden, H. M.: Information content of MOPITT CO profile retrievals: Temporal and geographical variability, J. Geophys. Res., 120(24), 12723–12738, https://doi.org/10.1002/2015JD024024, 2015.

Eresmaa, R., Letertre-Danczak, J., Lupu, C., Bormann, N., and McNally, A. P.: The assimilation of Cross-track Infrared Sounder radiances at ECMWF, Q. J. R. Meteorolog. Soc., 143(709), 3177–3188, 2017, https://doi.org/10.1002/qj.3171.

Frankenberg, C., Meirink, J. F., Bergamaschi, P., Goede, A. P. H., Heimann, M., Körner, S., Platt, U., van Weele, M., and Wagner, T.: Satellite chartography of atmospheric methane from SCIAMACHY on board ENVISAT: Analysis of the years 2003 and 2004, J. Geophys. Res., 111(D7), D07303, https://doi.org/10.1029/2005JD006235, 2006.

Fu, D., Bowman, K. W., Worden, H. M., Natraj, V., Worden, J. R., Yu, S., Veefkind, P., Aben, I., Landgraf, J., Strow, L., and Han, Y.: High-resolution tropospheric carbon monoxide profiles retrieved from CrIS and TROPOMI, Atmos. Meas. Tech., 9(6), 2567–2579, doi:10.5194/amt-9-2567-2016, 2016.

George, M., Clerbaux, C., Hurtmans, D., Turquety, S., Coheur, P.-F., Pommier, M., Hadji-Lazaro, J., Edwards, D. P., Worden, H., Luo, M., Rinsland, C., and McMillan, W.: Carbon monoxide distributions from the IASI/METOP mission: Evaluation with other space-borne remote sensors, Atmos. Chem. Phys., 9(21), 8317–8330, https://doi.org/10.5194/acp-9-8317-2009, 2009.

Hoffman, R. N., and Atlas, R.: Future observing system simulation experiments, Bull. Am. Meteorol. Soc., 97 (9), 1601–1616, https://doi.org/10.1175/BAMS-D-15-00200.1, 2016.

Hu, H., Landgraf, J., Detmers, R., Borsdorff, T., Aan de Brugh, J., Aben, I., Butz, A., and Hasekamp, O.: Toward global mapping of methane with TROPOMI: First results and intersatellite comparison to GOSAT, Geophys. Res. Lett., 45(8), 3682–3689, https://doi.org/10.1002/2018GL077259, 2018.

Irion, F. W., Kahn, B. H., Schreier, M. M., Fetzer, E. J., Fishbein, E., Fu, D., Kalmus, P., Wilson, R. C., Wong, S., and Yue, Q.: Single-footprint retrievals of temperature, water vapor and cloud properties from AIRS, Atmos. Meas. Tech., 11(2), 971–995, https://doi.org/10.5194/amt-11-971-2018, 2018.

Kuai, L., Worden, J., Kulawik, S., Bowman, K., Lee, M., Biraud, S. C., Abshire, J. B., Wofsy, S. C., Natraj, V., Frankenberg, C., Wunch, D., Connor, B., Miller, C., Roehl, C., Shia, R.-L., and Yung, Y.: Profiling tropospheric CO_2 using Aura TES and TCCON instruments, Atmos. Meas. Tech., 6(1), 63–79, https://doi.org/10.5194/amt-6-63-2013, 2013.

Kulawik, S. S., Osterman, G., Jones, D.B.A., and Bowman, K.W.: Calculation of altitude-dependent Tikhonov constraints for TES nadir retrievals, IEEE Trans. Geosci. Remote Sens., 44(5), 1334–1342, https://doi.org/10.1109/TGRS.2006.871206,2006.

Kulawik, S. S., Jones, D. B. A., Nassar, R., Irion, F. W., Worden, J. R., Bowman, K. W., Machida, T., Matsueda, H., Sawa, Y., Biraud, S. C., Fischer, M. L., and Jacobson, A. R.: Characterization of Tropospheric Emission Spectrometer (TES) CO_2 for carbon cycle science, Atmos. Chem. Phys., 10(12), 5601–5623, https://doi.org/10.5194/acp-10-5601-2010, 2010.

Landgraf, J., Aan de Brugh, J., Scheepmaker, R., Borsdorff, T., Hu, H., Houweling, S., Butz, A., Aben, I., and Hasekamp, O.: Carbon monoxide total column retrievals from TROPOMI shortwave infrared measurements, Atmos. Meas. Tech., 9(10), 4955–4975, https://doi.org/10.5194/amt-9-4955-2016, 2016.

https://doi.org/10.5194/amt-2021-290
Preprint. Discussion started: 5 October 2021
© Author(s) 2021. CC BY 4.0 License.

Ma, Z., Li, J., Han, W., Li, Z., Zeng, Q., Menzel, W. P., Schmit, T. J., Di, D., and Liu, C.-Y.: Four-dimensional wind fields from geostationary hyperspectral infrared sounder radiance measurements with high temporal resolution, Geophys. Res. Lett., 48(14), e2021GL093794, https://doi.org/10.1029/2021GL093794, 2021.

Meerdink, S. K., Hook, S. J., Roberts, D. A., and Abbott, E. A.: The ECOSTRESS spectral library version 1.0, Remote Sens. Environ., 230(111196), 1–8, https://doi.org/10.1016/j.rse.2019.05.015, 2019.

Nassar, R., Logan, J. A., Worden, H. M., Megretskaia, I. A., Bowman, K. W., Osterman, G. B., Thompson, A. M., Tarasick, D. W., Austin, S., Claude, H., Dubey, M. K., Hocking, W. K., Johnson, B. J., Joseph, E., Merrill, J., Morris, G. A., Newchurch, M., Oltmans, S. J., Posny, F., Schmidlin, F. J., Vomel, H., Whiteman, D. N., and Witte, J. C.: Validation of Tropospheric Emission Spectrometer (TES) nadir ozone profiles using ozonesonde measurements, J. Geophys. Res., 113(D15), D15S17, https://doi.org/10.1029/2007JD008819, 2008.

National Academies of Sciences, Engineering, and Medicine (NASEM): Thriving on Our Changing Planet: A Decadal Strategy for Earth Observation from Space, The National Academies Press, Washington, DC, https://doi.org/10.17226/24938, 2018.

Nelson, R. R., Crisp, D., Ott, L. E., and O'Dell, C. W.: High-accuracy measurements of total column water vapor from the Orbiting Carbon Observatory-2, Geophys. Res. Lett., 43(23), 12261–12269, https://doi.org/10.1002/2016GL071200, 2016.

Noël, S., Buchwitz, M., Bovensmann, H., and Burrows, J. P.: Validation of SCIAMACHY AMC-DOAS water vapour columns, Atmos. Chem. Phys., 5(7), 1835–1841, https://doi.org/10.5194/acp-5-1835-2005, 2005.

O'Dell, C. W., Eldering, A., Wennberg, P. O., Crisp, D., Gunson, M. R., Fisher, B., Frankenberg, C., Kiel, M., Lindqvist, H., Mandrake, L., Merrelli, A., Natraj, V., Nelson, R. R., Osterman, G. B., Payne, V. H., Taylor, T. R., Wunch, D., Drouin, B. J., Oyafuso, F., Chang, A., McDuffie, J., Smyth, M., Baker, D. F., Basu, S., Chevallier, F., Crowell, S. M. R., Feng, L., Palmer, P. I., Dubey, M., García, O. E., Griffith, D. W. T., Hase, F., Iraci, L. T., Kivi, R., Morino, I., Notholt, J., Ohyama, H., Petri, C., Roehl, C. M., Sha, M. K., Strong, K., Sussmann, R., Te, Y., Uchino, O., and Velazco, V. A.: Improved retrievals

https://doi.org/10.5194/amt-2021-290
Preprint. Discussion started: 5 October 2021
© Author(s) 2021. CC BY 4.0 License.

of carbon dioxide from the Orbiting Carbon Observatory-2 with the version 8 ACOS algorithm, Atmos. Meas. Tech., 11(12), 6539–6576, https://doi.org/10.5194/amt-2018-257, 2018.

Park, M., Randel, W. J., Kinnison, D. E., Garcia, R. R., and Choi, W.: Seasonal variation of methane, water vapor, and nitrogen oxides near the tropopause: Satellite observations and model simulations, J. Geophys. Res., 109(D3), https://doi.org/10.1029/2003JD003706, 2004.

Parker, R. J., Webb, A., Boesch, H., Somkuti, P., Barrio Guillo, R., Di Noia, A., Kalaitzi, N., Anand, J. S., Bergamaschi, P., Chevallier, F., Palmer, P. I., Feng, L., Deutscher, N. M., Feist, D. G., Griffith, D. W. T., Hase, F., Kivi, R., Morino, I., Notholt, J., Oh, Y.-S., Ohyama, H., Petri, C., Pollard, D. F., Roehl, C., Sha, M. K., Shiomi, K., Strong, K., Sussmann, R., Té, Y., Velazco, V. A., Warneke, T., Wennberg, P. O., and Wunch, D.: A decade of GOSAT proxy satellite CH_4 observations, Earth Syst. Sci. Data, 12(4), 3383–3412, https://doi.org/10.5194/essd-12-3383-2020, 2020.

Posselt, D. J., Wu, L., Schreier, M., Roman, J., Minamide, M., and Lambrigtsen, B.: Assessing the forecast impact of a geostationary microwave sounder using regional and global OSSEs, Mon. Weather Rev., conditionally accepted, 2021.

Rienecker, M. M., Suarez, M. J., Todling, R., Bacmeister, J., Takacs, L., Liu, H.-C., Gu, W., Sienkiewicz, M., Koster, R. D., Gelaro, R., Stajner, I., and Nielsen, J. E.: The GEOS-5 Data Assimilation System—Documentation of Versions 5.0.1, 5.1.0, and 5.2.0, NASA Tech. Rep. NASA/TM-2008-104606, 27, 2008.

Rodgers, C. D.: Inverse Methods for Atmospheric Sounding: Theory and Practice, World Scientific, Singapore, 2000.

Schneider, M., Ertl, B., Diekmann, C. J., Khosrawi, F., Röhling, A. N., Hase, F., Dubravica, D., García, O. E., Sepúlveda, E., Borsdorff, T., Landgraf, J., Lorente, A., Chen, H., Kivi, R., Laemmel, T., Ramonet, M., Crevoisier, C., Pernin, J., Steinbacher, M., Meinhardt, F., Deutscher, N. M., Griffith, D. W. T., Velazco, V. A., and Pollard, D. F.: Synergetic use of IASI and TROPOMI space borne sensors for generating a tropospheric methane profile product, Atmos. Meas. Tech. Discuss. [preprint], https://doi.org/10.5194/amt-2021-31, in review, 2021.

https://doi.org/10.5194/amt-2021-290
Preprint. Discussion started: 5 October 2021
© Author(s) 2021. CC BY 4.0 License.
Atmospheric Measurement Techniques
Open Access
Discussions

Schwantes, K. R., Cohen, D., Mantica, P., and Glumb, R. J.: Modeling noise equivalent change in radiance (NEdN) for the Crosstrack Infrared Sounder (CrIS), Proc. SPIE, 4486, 456–463, https://doi.org/10.1117/12.455128, 2002.

Smith, N., and Barnet, C. D.: CLIMCAPS observing capability for temperature, moisture, and trace gases from AIRS/AMSU and CrIS/ATMS, Atmos. Meas. Tech., 13(8), 4437–4459, https://doi.org/10.5194/amt-13-4437-2020, 2020.

Spurr, R., and Natraj, V.: A linearized two-stream radiative transfer code for fast approximation of multiple-scatter fields, J. Quant. Spectrosc. Radiat. Transfer, 112(16), 2630–2637, https://doi.org/10.1016/j.jqsrt.2011.06.014, 2011.

Teixeira, J., Piepmeier, J. R., Nehrir, A. R., Ao, C. O., Chen, S. S., Clayson, C. A., Fridlind, A. M., Lebsock, M., McCarty, W., Salmun, H., Santanello, J. A., Turner, D. D., Wang, Z., and Zeng, X.: Toward a Global Planetary Boundary Layer Observing System, https://science.nasa.gov/science-pink/s3fs-public/atoms/files/NASAPBLIncubationFinalReport.pdf.

Trent, T., Boesch, H., Somkuti, P., and Scott, N. A.: Observing water vapour in the planetary boundary layer from the short-wave infrared, Remote Sens., 10(9), 1469, https://doi.org/10.3390/rs10091469, 2018.

Worden, H. M., Deeter, M. N., Edwards, D. P., Gille, J. C., Drummond, J. R., and Nédélec, P. P.: Observations of near-surface carbon monoxide from space using MOPITT multispectral retrievals, J. Geophys. Res., 115(D18), D18314, https://doi.org/10.1029/2010JD014242, 2010.

Worden, H. M., Deeter, M. N., Frankenberg, C., George, M., Nichitiu, F., Worden, J., Aben, I., Bowman, K. W., Clerbaux, C., Coheur, P. F., de Laat, A. T. J., Detweiler, R., Drummond, J. R., Edwards, D. P., Gille, J. C., Hurtmans, D., Luo, M., Martínez-Alonso, S., Massie, S., Pfister, G., and Warner, J. X.: Decadal record of satellite carbon monoxide observations, Atmos. Chem. Phys., 13(2), 837–850, https://doi.org/10.5194/acp-13-837-2013, 2013.

Worden, J. R., Turner, A. J., Bloom, A., Kulawik, S. S., Liu, J., Lee, M., Weidner, R., Bowman, K., Frankenberg, C., Parker, R., and Payne, V. H.: Quantifying lower tropospheric methane concentrations

https://doi.org/10.5194/amt-2021-290
Preprint. Discussion started: 5 October 2021
© Author(s) 2021. CC BY 4.0 License.
Atmospheric Measurement Techniques Discussions

using GOSAT near-IR and TES thermal IR measurements, Atmos. Meas. Tech., 8(8), 3433–3445, https://doi.org/10.5194/amt-8-3433-2015, 2015.

Xi, X., Natraj, V., Shia, R.-L., Luo, M., Zhang, Q., Newman, S., Sander, S. P., and Yung, Y. L.: Simulated retrievals for the remote sensing of CO_2, CH_4, CO, and H_2O from geostationary orbit, Atmos. Meas. Tech., 8(11), 4817–4830, https://doi.org/10.5194/amt-8-4817-2015, 2015.

Xu, Z., Mace, G. G., and Posselt, D. J.: A method for assessing relative skill in retrieving cloud and precipitation properties in next generation cloud radar and radiometer orbiting observatories, J. Atmos. Oceanic Technol., 36(12), 2283–2306, https://doi.org/10.1175/JTECH-D-18-0204.1, 2019.

Yokota, T., Yoshida, Y., Eguchi, N., Ota, Y., Tanaka, T., Watanabe, H., and Maksyutov, S.: Global concentrations of CO_2 and CH_4 retrieved from GOSAT: First preliminary results, Sci. Online Lett. Atmos., 5(1), 160–163, https://doi.org/10.2151/sola.2009-041, 2009.

Zeng, X., Atlas, R., Birk, R. J., Carr, F. H., Carrier, M. J., Cucurull, L., Hooke, W. H., Kalnay, E., Murtugudde, R., Posselt, D. J., Russell, J. L., Tyndall, D. P., Weller, R. A., and Zhang, F.: Use of Observing System Simulation Experiments in the United States, Bull. Am. Meteorol. Soc., 101(8), E1427–E1438, https://doi.org/10.1175/BAMS-D-19-0155.1, 2020.

Zeng, Z.-C., Natraj, V., Xu, F., Pongetti, T. J., Shia, R.-L., Kort, E. A., Toon, G. C., Sander, S. P., and Yung, Y. L.: Constraining aerosol vertical profile in the boundary layer using hyperspectral measurements of oxygen absorption, Geophys. Res. Lett., 45(19), 10772–10780, https://doi.org/10.1029/2018gl079286, 2018.

Zeng, Z.-C., Zhang, Q., Natraj, V., Margolis, J. S., Shia, R.-L., Newman, S., Fu, D., Pongetti, T. J., Wong, K. W., Sander, S. P., Wennberg, P. O., and Yung, Y. L.: Aerosol scattering effects on water vapor retrievals over the Los Angeles Basin, Atmos. Chem. Phys., 17(4), 2495–2508, https://doi.org/10.5194/acp-17-2495-2017, 2017.

Zhang, Q., Natraj, V., Li, K.-F., Shia, R.-L., Fu, D., Pongetti, T. J., Sander, S. P., Roehl, C. M., and Yung, Y. L.: Accounting for aerosol scattering in the CLARS retrieval of column averaged CO_2 mixing ratios, J. Geophys. Res., 120(14), 7205–7218, https://doi.org/10.1002/2015jd023499, 2015.

© Author(s) 2021. CC BY 4.0 License.

Zhang, Q., Shia, R.-L., Sander, S. P., and Yung, Y. L.: XCO_2 retrieval error over deserts near critical surface albedo, Earth Space Sci., 3(2), 36–45, https://doi.org/10.1002/2015ea000143, 2016.

Zhang, Y., Jacob, D. J., Maasakkers, J. D., Sulprizio, M. P., Sheng, J.-X., Gautam, R., and Worden, J.: Monitoring global tropospheric OH concentrations using satellite observations of atmospheric methane, Atmos. Chem. Phys., 18(21), 15959–15973, https://doi.org/10.5194/acp-18-15959-2018, 2018.

© Author(s) 2021. CC BY 4.0 License.

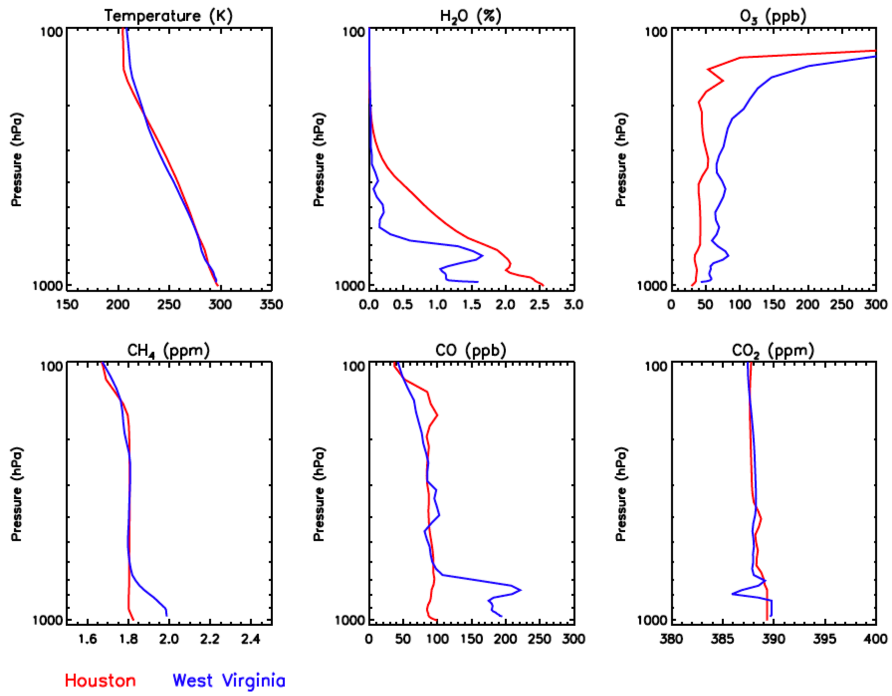

Figure 1: Scenarios considered in the simulations.

https://doi.org/10.5194/amt-2021-290
Preprint. Discussion started: 5 October 2021
© Author(s) 2021. CC BY 4.0 License.
Atmospheric Measurement Techniques Discussions

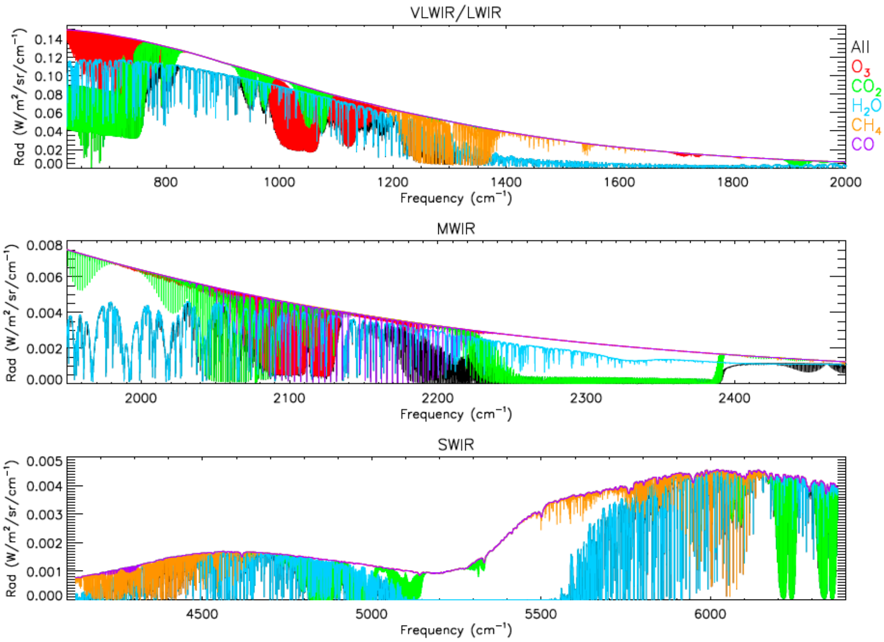

Figure 2. Simulated top of the atmosphere monochromatic radiances (black) in the 650–7000 cm^{-1} wavelength range for atmospheric profile near Houston. Also shown are radiances corresponding to (red) O_3, (green) CO_2, (blue) H_2O, (orange) CH_4, and (purple) CO absorption.

https://doi.org/10.5194/amt-2021-290
Preprint. Discussion started: 5 October 2021
© Author(s) 2021. CC BY 4.0 License.
Atmospheric Measurement Techniques Discussions

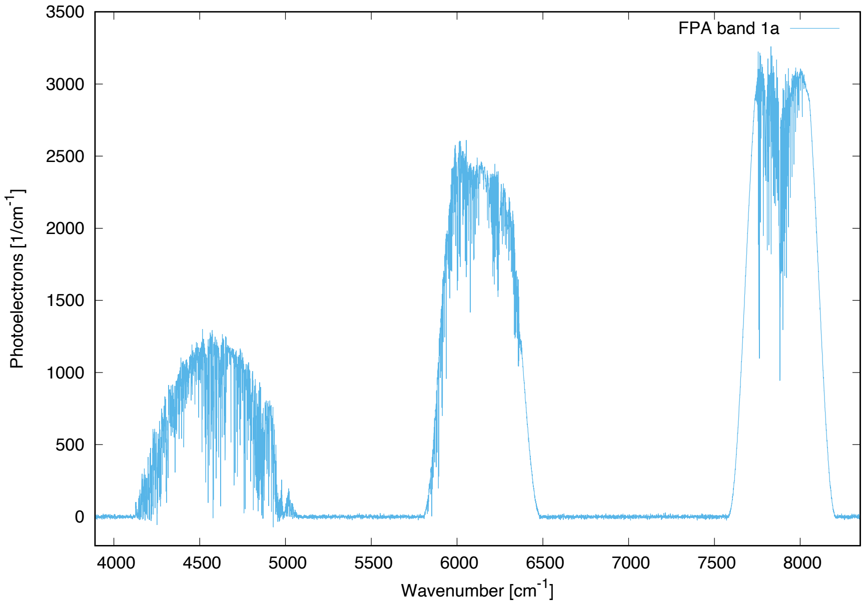

Figure 3: Simulated JPL GEO-IR Sounder spectrum in the SWIR domain. The SWIR domain is sub-divided into discrete bands using a triple-band interference filter to maximize the SNR in spectral regions of interest (CO_2, CH_4, CO, H_2O, and O_2).

https://doi.org/10.5194/amt-2021-290
Preprint. Discussion started: 5 October 2021
© Author(s) 2021. CC BY 4.0 License.
Atmospheric Measurement Techniques Discussions

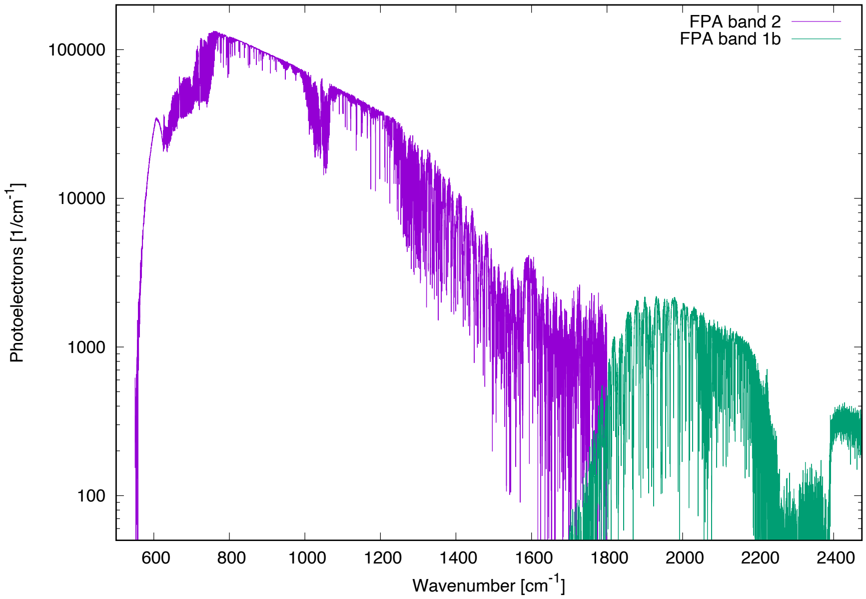

Figure 4: Simulated JPL GEO-IR Sounder spectrum in the VLWIR, LWIR and MWIR domains. Note the logarithmic scale.

https://doi.org/10.5194/amt-2021-290
Preprint. Discussion started: 5 October 2021
© Author(s) 2021. CC BY 4.0 License.

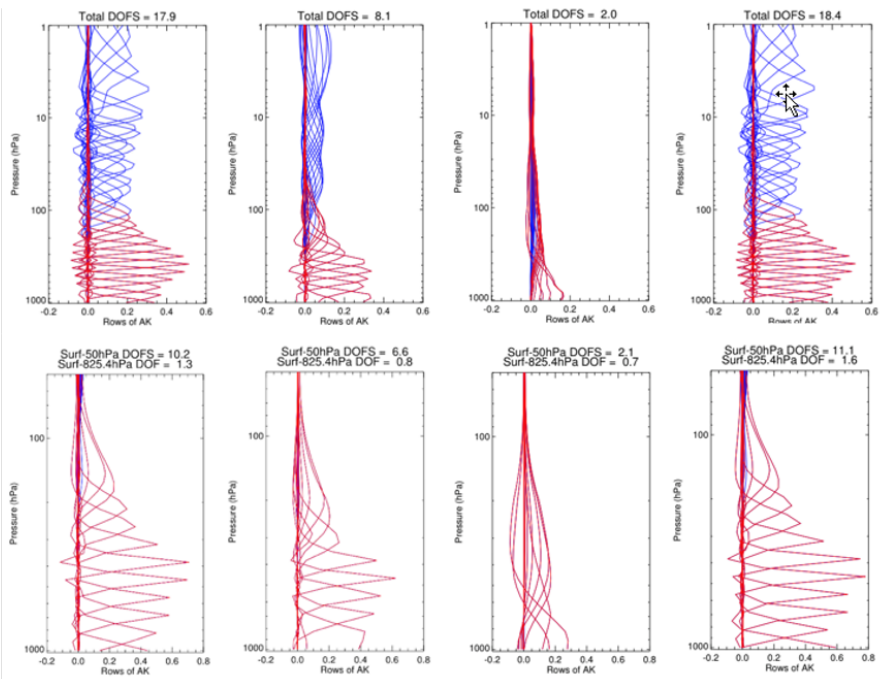

Figure 5: Plots of averaging kernel rows for (top) TATM and (bottom) H_2O. The spectral ranges are (from left to right) VLWIR+LWIR, MWIR, SWIR, and VLWIR+LWIR+MWIR+SWIR. These results are for the Houston case. The blue and red lines refer to averaging kernel rows for pressure levels above and below 100 hPa, respectively.

https://doi.org/10.5194/amt-2021-290
Preprint. Discussion started: 5 October 2021
© Author(s) 2021. CC BY 4.0 License.

Atmospheric Measurement Techniques
Discussions

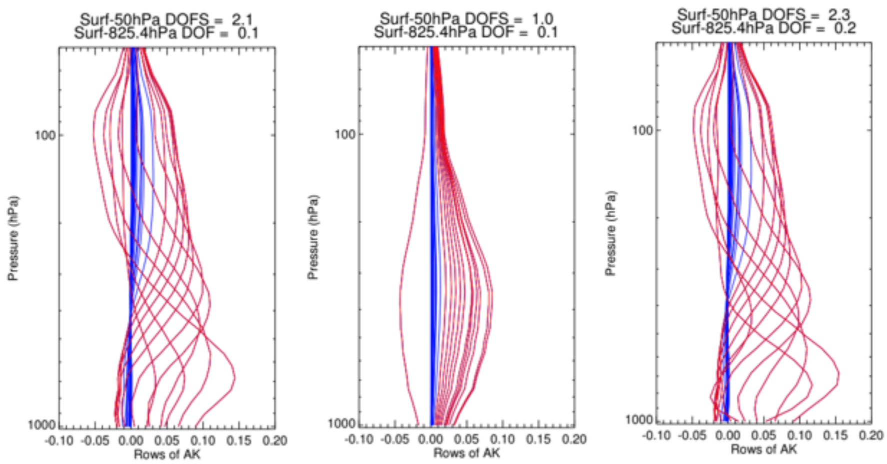

Figure 6: Plots of averaging kernel rows for CO retrievals. The spectral ranges are (from left to right) MWIR, SWIR, and MWIR+SWIR. These results are for the West Virginia case. The color scheme is the same as in Figure 5.

https://doi.org/10.5194/amt-2021-290
Preprint. Discussion started: 5 October 2021
© Author(s) 2021. CC BY 4.0 License.

Atmospheric Measurement Techniques
Discussions

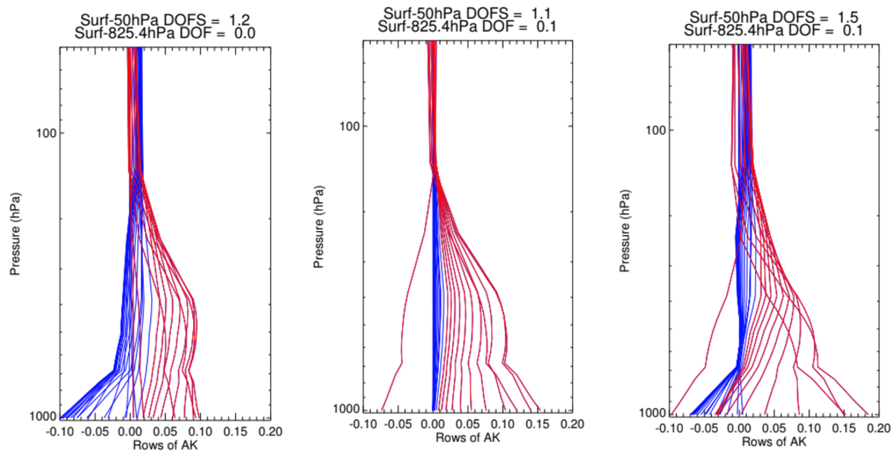

Figure 7: Plots of averaging kernel rows for CO_2 retrievals. The spectral ranges are (from left to right) VLWIR+MWIR, SWIR, and VLWIR+MWIR+SWIR. These results are for the West Virginia case. The color scheme is the same as in Figure 5.

https://doi.org/10.5194/amt-2021-290
Preprint. Discussion started: 5 October 2021
© Author(s) 2021. CC BY 4.0 License.

Atmospheric Measurement Techniques
Discussions

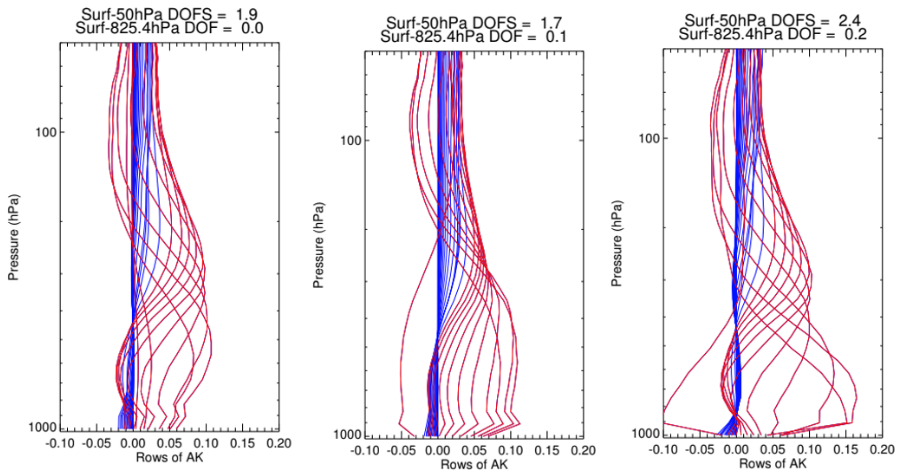

Figure 8: Plots of averaging kernel rows for CH_4 retrievals. The spectral ranges are (from left to right) LWIR, SWIR, and LWIR+SWIR. These results are for the West Virginia case. The color scheme is the same as in Figure 5.

https://doi.org/10.5194/amt-2021-290
Preprint. Discussion started: 5 October 2021
© Author(s) 2021. CC BY 4.0 License.

Table 1. Spectral ranges and their designations used in this study.

Designation	**Spectral Range (μm)**	**Spectral Range (cm^{-1})**
VLWIR	>10	<1,000
LWIR	5–10	1,000–2,000
MWIR	3–5	2,000–3,333
SWIR	1–3	3,333–10,000
TIR	>3	<3,333

https://doi.org/10.5194/amt-2021-290
Preprint. Discussion started: 5 October 2021
© Author(s) 2021. CC BY 4.0 License.

Table 2. Current and planned missions making spaceborne, spectrally resolved measurements of TIR and SWIR radiances. Note that MOPITT was designed to also offer measurements of CH_4, although that did not materialize (hence the gray shading).

Orbit	Instrument/mission	T profile	H_2O		CO		CH_4		CO_2	
		TIR	TIR	SWIR	TIR	SWIR	TIR	SWIR	TIR	SWIR
LEO	Hyperspectral TIR sounders (AIRS, CrIS, IASI, IASI-NG, TES)	Y	Y		Y		Y		Y	
	MOPITT				Y	Y				
	GOSAT, GOSAT-2	Y	Y	Y	Y		Y	Y	Y	Y
	OCO-2/OCO-3			Y						Y
	TROPOMI			Y		Y		Y		
	TANSAT			Y						Y
GEO	IRS	Y	Y		Y		Y		Y	
	GIIRS	Y	Y		Y		Y		Y	
	GeoCarb			Y		Y		Y		Y
	JPL GEO-IR Sounder	Y	Y	Y	Y	Y	Y	Y	Y	Y

© Author(s) 2021. CC BY 4.0 License.

Table 3. Spectral ranges used in this study for simulated retrievals of CO, CH_4 and CO_2.

Molecule	Spectral Ranges (cm^{-1})	Relevant For
Carbon monoxide (CO)	2000–2250 4210–4350	Air quality and carbon cycle (combustion and fire emissions)
Methane (CH_4)	1210–1380 4210–4350 6000–6150	Greenhouse gas monitoring and carbon cycle (wetlands, oil and gas, agriculture)
Carbon dioxide (CO_2)	650–1100 2250–2450 4810–4900 6170–6290	Greenhouse gas monitoring and carbon cycle (human emissions, status of land and ocean carbon sinks)

759

https://doi.org/10.5194/amt-2021-290
Preprint. Discussion started: 5 October 2021
© Author(s) 2021. CC BY 4.0 License.

Table 4. Comparison of JPL GEO-IR Sounder with other state-of-the-art instruments.

Instrument	GIIRS	IRS	CrIS	JPL GEO-IR Sounder
Status	In space	2023 launch	In space	This study
Nationality	China	EU	US	US
Orbit	GEO	GEO	Polar	GEO
Longitude (°)	104.7 E	0–45 E	N/A	75–137 W
Spacecraft	Dedicated	Dedicated	Dedicated	Hosted payload
GSD, nadir (km)	16	4	14	4.2 (binned), 2.1 (native)
Spectral range (cm^{-1} unless otherwise indicated)	700–1130 1650–2250 0.55–0.75 µm	680–1210 1600–2250	650 – 1095 1210 – 1750 2155 – 2550	650–10,000*
Resolution (cm^{-1})	0.625	0.625	0.625	NSR** = 0.625, FSR = 0.1
Full Disk Revisit Time (hr)	2–3	1	12	0.2

**FTS instrument capability*
*** NSR = Nominal Spectral Resolution. FSR = Full Spectral Resolution. FSR mode decreases retrieval biases caused by interfering absorbers*

https://doi.org/10.5194/amt-2021-290
Preprint. Discussion started: 5 October 2021
© Author(s) 2021. CC BY 4.0 License.

Table 5. DOFS for TATM retrievals for three spectral (MOPD) and two spatial (GSD) resolution scenarios. The values shown here are for the Houston profile.

Frequency Domain	DOFS (MOPD = 5 cm)		DOFS (MOPD = 2 cm)		DOFS (MOPD = 0.8 cm)	
	2.1 km GSD	4.2 km GSD	2.1 km GSD	4.2 km GSD	2.1 km GSD	4.2 km GSD
VLWIR+LWIR	13.6	17.6	14.2	17.9	14.3	17.9
MWIR	5.1	7.9	5.8	8.3	6	8.1
VLWIR+LWIR+MWIR	13.8	17.8	14.4	18.1	14.5	18.1
SWIR	0.2	1.6*	0.3	1.8*	0.4	2.0*
VLWIR+LWIR+MWIR+SWIR	13.8	17.9*	14.6	18.3*	14.7	18.4*

* Instrument noise is reduced by a factor of 5 through footprint averaging for the SWIR only, providing an effective GSD of 21 km.

https://doi.org/10.5194/amt-2021-290
Preprint. Discussion started: 5 October 2021
© Author(s) 2021. CC BY 4.0 License.

Atmospheric Measurement Techniques Discussions

Table 6: Same as Table 5 but for H_2O

Frequency Domain	DOFS (MOPD = 5 cm)		DOFS (MOPD = 2 cm)		DOFS (MOPD = 0.8 cm)	
	2.1 km GSD	4.2 km GSD	2.1 km GSD	4.2 km GSD	2.1 km GSD	4.2 km GSD
VLWIR+LWIR+	7.9	11.2	8.2	11.3	8.2	11.2
MWIR	4.6	6.9	5.0	7.3	4.6	6.6
VLWIR+LWIR+ MWIR	8.3	11.8	8.8	12.1	8.6	11.9
SWIR	1.2	2.2*	1.3	2.1*	1.4	2.1*
VLWIR+LWIR+ MWIR+SWIR	8.3	12.1*	8.9	12.3*	8.7	12.1*

* Instrument noise is reduced by a factor of 5 through footprint averaging for the SWIR only, providing an effective GSD of 21 km.

https://doi.org/10.5194/amt-2021-290
Preprint. Discussion started: 5 October 2021
© Author(s) 2021. CC BY 4.0 License.

Table 7. Trace gas retrieval configurations and DOFS for the West Virginia profile. TATM and H_2O are simultaneously retrieved when listed.

Retrieved Species	Frequency Domain	DOFS (MOPD = 2 cm)		DOFS (MOPD = 0.8 cm)	
		2.1 km GSD	4.2 km GSD	2.1 km GSD	4.2 km GSD
O_3 (TATM, H_2O)	LWIR	3.5	4.0	3.4	4.0
CO	MWIR	1.7	2.1	1.6	2.1
	SWIR	0.08	0.96*	0.1	0.96*
	MWIR+SWIR	1.7	2.3*	1.7	2.3*
CH_4 (TATM, H_2O)	LWIR	1.5	2.0	1.6	2.1
	SWIR	0.7	1.9*	0.8	1.9*
	LWIR+SWIR	1.6	2.7*	1.8	2.8*
CO_2 (TATM, H_2O)	VLWIR	1.0	1.5	1.1	1.6
	VLWIR+MWIR	1.0	1.5	1.2	1.6
	SWIR	0.3	1.1*	0.4	1.1*
	VLWIR+MWIR +SWIR	1.0	1.7*	1.2	1.9*

* Instrument noise is reduced by a factor of 5 through footprint averaging for the SWIR only, providing an effective GSD of 21 km.

https://doi.org/10.5194/amt-2021-290
Preprint. Discussion started: 5 October 2021
© Author(s) 2021. CC BY 4.0 License.

Table 8. Estimates of total and precision errors for JPL GEO-IR Sounder, CrIS and AIRS TATM and H_2O retrievals in the troposphere. Note that data used for CrIS and AIRS retrievals were obtained near Houston, Texas in August 2020. Averaged retrieved cloud optical depths are limited to less than 0.1, consistent with mostly clear-sky conditions.

	TATM		H_2O (lower-mid troposphere)	
	Total Error	Precision	Total Error	Precision
JPL GEO-IR Sounder (MWIR-only)	0.5–1.5 K	0.2–0.6 K	~8%	~5%
JPL GEO-IR Sounder (Entire spectral range)	0.3–1 K	0.1–0.3 K	~5%	~3%
CrIS	0.5–1.5 K	0.2–0.3 K	10–13%	2–3%
AIRS	0.5–1.2 K	~0.3 K	15–30%	2–5%